

# Photoinduced Water Oxidation at the Aqueous GaN (10 $\bar{1}$ 0) Interface: Deprotonation Kinetics of the First Proton-Coupled Electron-Transfer Step

Mehmed Z. Ertem,<sup>\*,†,‡,||</sup> Neerav Kharche,<sup>\*,†,||</sup> Victor S. Batista,<sup>‡</sup> Mark S. Hybertsen,<sup>§</sup> John C. Tully,<sup>‡</sup> and James T. Muckerman<sup>\*,†</sup>

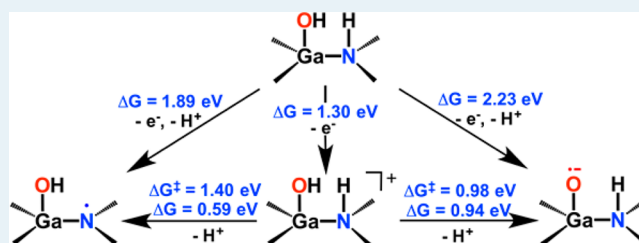
<sup>†</sup>Chemistry Department and <sup>§</sup>Center for Functional Nanomaterials, Brookhaven National Laboratory, Upton, New York 11973-5000, United States

<sup>‡</sup>Department of Chemistry, Yale University, P.O. Box 208107, New Haven, Connecticut 06520, United States

## Supporting Information

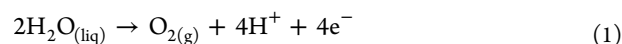
**ABSTRACT:** Photoelectrochemical water splitting plays a key role in a promising path to the carbon-neutral generation of solar fuels. Wurtzite GaN and its alloys (e.g., GaN/ZnO and InGaN) are demonstrated photocatalysts for water oxidation, and they can drive the overall water splitting reaction when coupled with co-catalysts for proton reduction. The present work investigates the water oxidation mechanism on the prototypical GaN (10 $\bar{1}$ 0) surface using a combined ab initio molecular dynamics and molecular cluster model approach taking into account the role of water dissociation and hydrogen bonding within the first solvation shell of the hydroxylated surface. The investigation of free-energy changes for the four proton-coupled electron-transfer (PCET) steps of the water oxidation mechanism shows that the first PCET step for the conversion of  $-\text{Ga}-\text{OH}$  to  $-\text{Ga}-\text{O}^{\bullet-}$  requires the highest energy input. The study further examines the sequential PCETs, with the proton transfer (PT) following the electron transfer (ET), and finds that photogenerated holes localize on surface  $-\text{NH}$  sites, and the calculated free-energy changes indicate that PCET through  $-\text{NH}$  sites is thermodynamically more favorable than  $-\text{OH}$  sites. However, proton transfer from  $-\text{OH}$  sites with subsequent localization of holes on oxygen atoms is kinetically favored owing to hydrogen bonding interactions at the GaN (10 $\bar{1}$ 0)–water interface. The deprotonation of surface  $-\text{OH}$  sites is found to be the limiting factor for the generation of reactive oxyl radical ion intermediates and consequently for water oxidation.

**KEYWORDS:** water oxidation, density functional theory, GaN, photocatalysis, aqueous interface, AIMD



## INTRODUCTION

Water splitting powered by sunlight provides a carbon-neutral framework for the generation of solar fuels.<sup>1–3</sup> The design and synthesis of more efficient solar water splitting systems require a deeper understanding of the key process of the catalytic oxidation of water to molecular oxygen,<sup>4</sup> which involves the transfer of four protons and four electrons with concomitant O–O bond formation (eq 1):



Domen and co-workers synthesized wurtzite GaN/ZnO alloys as photocatalysts for water oxidation, which, when coupled with proton reduction co-catalysts, split  $\text{H}_2\text{O}$  into  $\text{O}_2$  and  $\text{H}_2$ .<sup>5–7</sup> The holes generated by absorption of light migrate to the GaN/ZnO nanoparticle surface, where oxidation of water to molecular oxygen occurs ( $2\text{H}_2\text{O} + 4\text{h}^+ \rightarrow \text{O}_2 + 4\text{H}^+$ ), whereas the electrons are consumed on the co-catalyst surface for the proton reduction reaction ( $4\text{H}^+ + 4\text{e}^- \rightarrow 2\text{H}_2$ ).<sup>7</sup> The net outcome is the use of four electron–hole pairs generated by incident photons to split two  $\text{H}_2\text{O}$  into  $\text{O}_2$  and two  $\text{H}_2$ . Because

GaN/ZnO alloys have narrower band gaps than either GaN or ZnO and have significant visible light absorption,<sup>8–11</sup> they could be employed as photoanodes in photoelectrochemical cells for solar water splitting.<sup>5,6,12</sup> Additionally, successful water splitting has also been demonstrated using GaN<sup>13,14</sup> and InGaN alloys.<sup>15</sup> Therefore, it is crucial to understand the fundamental features of water oxidation on the prototypic GaN surface.

In earlier work, Shen et al.<sup>16</sup> studied the water oxidation mechanism on the GaN (10 $\bar{1}$ 0) surface using cluster models generated from snapshots of ab initio molecular dynamics (AIMD) simulations of the GaN (10 $\bar{1}$ 0)–water interface.<sup>17</sup> The proposed mechanism consists of four proton-coupled electron-transfer (PCET) steps resembling those proposed earlier by Norskov et al. for other materials.<sup>18,19</sup> The highest energy requirement was found to be associated with the first PCET step leading to the generation of the reactive oxyl radical ion intermediate from a surface-bound hydroxide ion ( $^*\text{OH}^-$

Received: January 12, 2015

Revised: February 20, 2015

Published: March 4, 2015

$\rightarrow *O^{\bullet-} + e^- + H^+$ ). Recently, Akimov et al.<sup>20</sup> investigated the evolution of a photogenerated hole and the following proton-transfer step at the GaN (10 $\bar{1}0$ )–water interface by combining non-adiabatic molecular dynamics and time-dependent density functional theory (TDDFT) methods and found that the hole localizes on the surface nitrogen atoms and promotes proton transfer from –NH groups to either surface –OH or bulk H<sub>2</sub>O molecules.<sup>20</sup> This observation is quite interesting and presents a puzzle because the splitting of water and formation of an O–O bond require the hole to be localized on an oxygen atom.<sup>16</sup>

Turning to GaN/ZnO alloys, Kharche et al.<sup>21</sup> recently studied the structure of aqueous interfaces of the nonpolar (10 $\bar{1}0$ ) and (1 $\bar{2}10$ ) wurtzite facets of the 1:1 GaN/ZnO alloy using AIMD simulations. This study found that, similar to the GaN (10 $\bar{1}0$ ) surface, water also dissociates spontaneously on the (10 $\bar{1}0$ ) and (1 $\bar{2}10$ ) surfaces of the GaN/ZnO alloy. The degree of water dissociation, however, is dependent on the surface composition. That work also reports similar hydrogen bonding patterns of the surface-adsorbed protons and hydroxide ions with the bulk water layer at the aqueous interfaces of GaN and GaN/ZnO alloys,<sup>21</sup> which suggests that the water oxidation mechanism on the GaN/ZnO alloy surfaces should closely resemble that on the GaN surface.

In the present work, we employ AIMD simulations to investigate the atomic structure of the GaN (10 $\bar{1}0$ )–water interface and use snapshots from these simulations to investigate the water oxidation mechanism following PCET steps using molecular cluster models. In addition to the coupled PCETs, we also investigate sequential electron-transfer (ET) followed by proton-transfer (PT) steps. We find that photogenerated holes localize on surface –NH sites, confirming the result from refs 20 and 21 that the top of the valence band at the GaN (10 $\bar{1}0$ )–aqueous interface consists of N(2p) states and, furthermore, that the PCET through –NH sites is thermodynamically more favorable than that through –OH sites. However, when we investigate the pathway for proton transfer, we find that proton transfer from –OH sites and subsequent localization of holes on oxygen atoms occur at a faster rate, compared to the –NH sites, because of hydrogen bonding interactions at the GaN (10 $\bar{1}0$ )–water interface. This provides an explanation for how the holes localize on oxygen atoms to promote water oxidation catalysis. Our calculations show that the deprotonation of surface –OH sites is the limiting step for the generation of reactive oxyl radical ion intermediates, which are required for the critical step of O–O bond formation through nucleophilic attack by water molecules.

## ■ COMPUTATIONAL METHODS

**Ab Initio Molecular Dynamics.** The GaN–water interface is simulated using a repeated supercell in which a 12-layer slab of (10 $\bar{1}0$ ) oriented wurtzite GaN with a 3 × 2 lateral cell alternates with a water-filled region containing 81 water molecules (Figure 1a,b). The MD trajectory for this supercell was simulated in our earlier study.<sup>22</sup> The simulation protocol<sup>21,22</sup> is summarized here for completeness. In brief, DFT calculations are carried out using the projector augmented wave (PAW) method<sup>23</sup> as implemented in VASP.<sup>24,25</sup> On the basis of prior experience,<sup>8</sup> the semicore 3d levels for Ga are explicitly treated, and the DFT+*U* method within the Dudarev formulation<sup>26</sup> is employed with  $U_{\text{Ga}} = 3.9$  eV for the 3d orbitals. The Brillouin zone is sampled only at the  $\Gamma$ -point, which is sufficient for the large supercells involved in this study. The

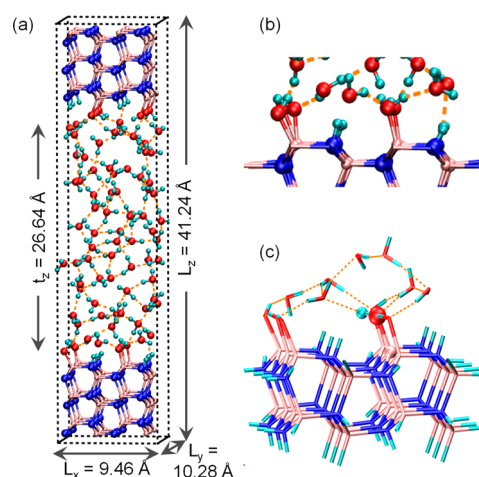


**Figure 1.** Atomistic schematics of (a) a snapshot from the equilibrated portion of the MD simulation illustrating the unit cell, (b) a magnified view of the aqueous interface illustrating interface hydrogen bonds, and (c) the cluster model highlighting the reactive –Ga–OH site in the ball-and-stick representation. The hydrogen bond network is depicted by the dashed orange lines.

Born–Oppenheimer MD simulations are performed using a Nose–Hoover thermostat and a Verlet integrator with a time step of 0.5 fs. The functional optB88-vdW,<sup>27,28</sup> including long-range van der Waals interactions, together with a slightly elevated temperature ( $T = 350$  K), gives an accurate O–O pair distribution function and diffusivity.<sup>21,22</sup> Converged results require a cutoff energy of 600 eV. The MD simulation is run for 16 ps, and structural analysis is performed for a 6 ps equilibrated window.

**Molecular Cluster Model.** The GaN (10 $\bar{1}0$ ) surface model was built from a representative structure obtained from ab initio molecular dynamics simulations, as detailed in the previous section. The 3 × 2 GaN (10 $\bar{1}0$ ) surface model contains 28 Ga and 28 N atoms, 12 of which form –Ga–OH and –NH surface species upon dissociation of 6 H<sub>2</sub>O molecules (Figure 1c). In addition to that, 7 H<sub>2</sub>O molecules are included in the model to preserve the H-bonding interactions and first-shell solvation effects. The dangling bonds formed at terminal positions of the model were passivated with H atoms to complete the coordination number of Ga and N atoms. The details of the comparison of the present cluster model with previous models in ref 16 are presented in the Supporting Information.

All geometries were fully optimized at the M11-L level of density functional theory<sup>29,30</sup> with the SMD aqueous continuum solvation model<sup>31</sup> surrounding the entire cluster using the Stuttgart ECP28MWB contracted pseudopotential basis set on Ga<sup>32,33</sup> and the 6-31G(d) 5d basis set<sup>34</sup> on all other atoms. Nonanalytical integrals were evaluated using the *integral=grid=ultrafine* option as implemented in the Gaussian 09 software package.<sup>35</sup> The nature of all stationary points was verified by analytic computation of vibrational frequencies, which were also used for the computation of zero-point vibrational energies, molecular partition functions, and determining the reactants and products associated with each transition-state structure (by following the normal modes associated with imaginary frequencies). The transition state structures were optimized using the “opt=(ts,noeigentest)” keyword starting with guess structures, and final optimized transition state structures were verified to be associated with a single imaginary frequency. Partition functions were used in the

computation of 298 K thermal contributions to the free energy employing the usual ideal-gas, rigid-rotator, harmonic oscillator approximation.<sup>36</sup> Free-energy contributions were added to single-point M11-L electronic energies computed at the optimized geometries obtained with the above-mentioned 6-31G(d) basis set using the SDD basis set on Ga and the 6-311+G(2df,p) 5d, 7f basis set on all other atoms to arrive at final composite free energies.

As mentioned above, solvation effects associated with bulk water as solvent were accounted for using the SMD aqueous continuum solvation model.<sup>31</sup> A 1 M standard state was used for all species in solution; thus, an adjustment for the 1 atm to 1 M standard-state concentration change of  $RT \ln(24.5)$ , or 1.89 kcal/mol, was added to the computed free energies. In the case of water, the 1 atm gas-phase free energy is adjusted by the sum of a 1 atm to 1 M (1.89 kcal/mol) and 1 M to 55.6 M (2.38 kcal/mol) standard-state concentration change, 4.27 kcal/mol in total, and the experimental 1 M to 1 M self-solvation free energy, -6.32 kcal/mol, yielding an overall correction of -2.05 kcal/mol to the gas-phase free energy. The 1 M to 1 M solvation free energy of the proton was taken from experiment as -265.9 kcal/mol.<sup>37-40</sup> The free-energy changes are reported at pH 4.0 as representative of the range of experimental conditions<sup>5,6</sup> and denoted  $\Delta G^{*}$ , which includes a correction of -5.46 kcal/mol ( $-4RT \ln(10)$ ) for the free energy of the solvated proton.

Standard reduction potentials were calculated for various possible redox couples to assess the energetic accessibility of different intermediates at various oxidation states. For a redox reaction of the form



where Ox and Red denote the oxidized and reduced states of the redox couple, respectively, and  $n$  is the number of electrons involved in redox reaction, the reduction potential  $E_{\text{Ox/Red}}$  relative to NHE was computed as

$$E_{\text{Ox/Red}} = - \frac{\Delta G_{\text{Ox/Red}}^{*} - \Delta G_{\text{NHE}}^{\circ}}{nF} = - \frac{\Delta G_{\text{Ox/Red}}^{*}}{nF} + \frac{\Delta G_{\text{NHE}}^{*}}{F} \quad (3)$$

where  $\Delta G_{\text{Ox/Red}}^{*}$  is the free-energy change associated with eq 2 (using Boltzmann statistics for the electron),  $\Delta G_{\text{NHE}}^{*}$  is the free-energy change associated with



which is -4.28 eV with Boltzmann statistics for the electron,<sup>39,41,42</sup> and  $F$  is the Faraday constant.

To investigate the choice of density functional on reaction energetics, we performed single-point calculations at the B3LYP<sup>43</sup> level of theory using M11-L optimized structures of cluster models. Free-energy contributions from M11-L calculations were added to single-point B3LYP electronic energies computed with the SDD basis set on Ga and the 6-311+G(2df,p) 5d, 7f basis set on all other atoms to arrive at final free energies. The comparison of computed potentials for PCET steps of the proposed water oxidation mechanism indicate close agreement between M11-L and B3LYP for all of the steps (Scheme S2 and Table S1). In addition to the above, we performed single-point B3LYP electronic energies computed with the SDD basis set on Ga and the 6-311G(d,p) 5d, 7f basis set on all other atoms to compare with potentials computed by Shen et al.<sup>16</sup> in an earlier work (Table S2).

## RESULTS AND DISCUSSION

### Atomic Structure of the GaN (10 $\bar{1}0$ )-Water Interface.

Ab initio MD simulations allow us to characterize the atomic structure of the aqueous interface of the (10 $\bar{1}0$ ) surface of GaN in the resting (or “dark”) state. In agreement with earlier studies,<sup>16,21,22,44</sup> all adsorbed water molecules on the GaN surface are found to dissociate spontaneously into protons ( $\text{H}^{+}$ ) and hydroxide ions ( $\text{OH}^{-}$ ) during the MD run. Surface N atoms accept protons from the dissociated water molecules, forming -NH species, whereas the corresponding hydroxide ions bond with surface Ga atoms, forming -Ga-OH species. Thus, under ambient conditions the aqueous GaN (10 $\bar{1}0$ ) interface is fully hydroxylated (Figure 1a,b).

The strong perturbation in the structure of water, induced by the water dissociation resulting from the acid-base chemistry at the solvated GaN surface, extends up to 3 Å distance from the surface. The water layer beyond 3 Å distance from the surface exhibits a bulk-like hydrogen bond network and oxygen-oxygen radial distribution function.<sup>22</sup> In the bulk water region, the average density is 1.08 g/cm<sup>3</sup>, slightly larger than the ambient density of water (1.00 g/cm<sup>3</sup>). The interfacial water layer up to 3 Å distance from the surface includes surface adsorbed protons and hydroxide ions as well as the first solvation shell of the hydroxylated surface (Figure 1b). These species are explicitly included in our cluster model (Figure 1c).

The hydroxylated surface interacts with the water layer via a hydrogen bond network, indicated by the dashed orange lines in Figure 1a,b. An adsorbed hydroxide ion can form at most one donor and two acceptor hydrogen bonds, whereas an adsorbed proton can be involved in at most only one donor hydrogen bond. The number of hydrogen bonds of each kind depends on how they are defined. Here, two species are considered to be hydrogen bonded when the distance between donor (D) and acceptor (A) atoms,  $d_{\text{D-A}}$ , is <3 Å and the DHA angle is >140°. Quantitative analysis of the equilibrated portion of the MD trajectory over long periods (ca. 6 ps) indicates that substantially more hydrogen bonds are formed by the -Ga-OH species compared to the -NH species (Figure 2). Similar quantitative results for  $d_{\text{D-A}} = 3.25$  and 3.5 Å are included in Figure S1 in the Supporting Information. The fewer donor hydrogen bonds involving the -NH species with smaller  $d_{\text{D-A}}$  indicates that these hydrogen bonds are relatively weaker

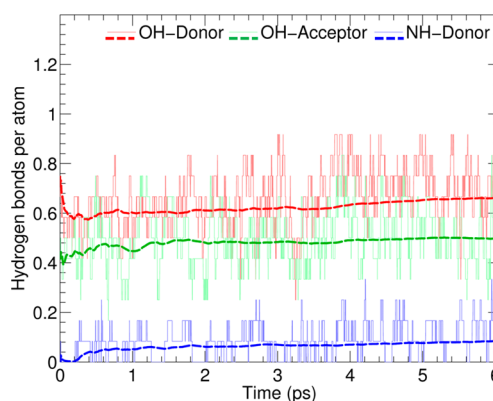


**Figure 2.** Time dependence of the number of hydrogen bonds between the hydroxylated GaN surface and the bulk water layer from the equilibrated portion of the MD simulation. Instantaneous and time-averaged traces are depicted by thin continuous and thick dashed lines, respectively.

Table 1. System and Reservoir Species for the Various Steps of the Water Oxidation Catalytic Cycle<sup>a</sup>

system	reservoir	$G_{\text{sys}}^{*'} \text{ (Ha)}$	$G_{\text{res}}^{*'} \text{ (Ha)}$	$G_{\text{total}}^{*'} \text{ (Ha)}$	rel $\Delta G^{*'} \text{ (eV)}$	rel $\Delta G^{*'} \text{ (eV vs NHE)}$ <sup>d</sup>
–Ga–OH	2H <sub>2</sub> O <sub>(liq)</sub>	–2611.9859	–152.8648	–2764.8507	0.00	0.00
–Ga–O <sup>•-</sup>	2H <sub>2</sub> O <sub>(liq)</sub> , H <sup>+</sup> , e <sup>-</sup>	–2611.3073	–153.3042	–2764.6114	6.51	2.23
–Ga–OOH	H <sub>2</sub> O <sub>(liq)</sub> , 2H <sup>+</sup> , 2e <sup>-</sup>	–2687.1083	–77.3112	–2764.4195	5.22	0.94
–Ga–OO <sup>•-</sup>	H <sub>2</sub> O <sub>(liq)</sub> , 3H <sup>+</sup> , 3e <sup>-</sup>	–2686.4785	–77.7506	–2764.2291	5.18	0.90
–Ga–OH	O <sub>2(g)</sub> , 4H <sup>+</sup> , 4e <sup>-</sup>	–2611.9859	–152.0805	–2764.0664	4.43	0.15
net sys rxn: –Ga–OH → –Ga–OH	net res rxn: 2H <sub>2</sub> O <sub>(liq)</sub> → O <sub>2(g)</sub> + 4H <sup>+</sup> + 4e <sup>-</sup>				21.34	1.06

<sup>a</sup>Associated free energies ( $G^{*}$ ) in units of hartree and free-energy changes ( $\Delta G^{*}$ ) in units of eV from cluster model calculations are reported at pH 4.0. <sup>b</sup>Absolute free energies with respect to zero on the vacuum reference potential scale. <sup>c</sup>Values of absolute free energy with respect to zero on the vacuum reference potential scale relative to –Ga–OH + 2H<sub>2</sub>O<sub>(liq)</sub>. <sup>d</sup>Values of absolute free energy with respect to zero on the normal hydrogen electrode scale relative to –Ga–OH + 2H<sub>2</sub>O<sub>(liq)</sub>.

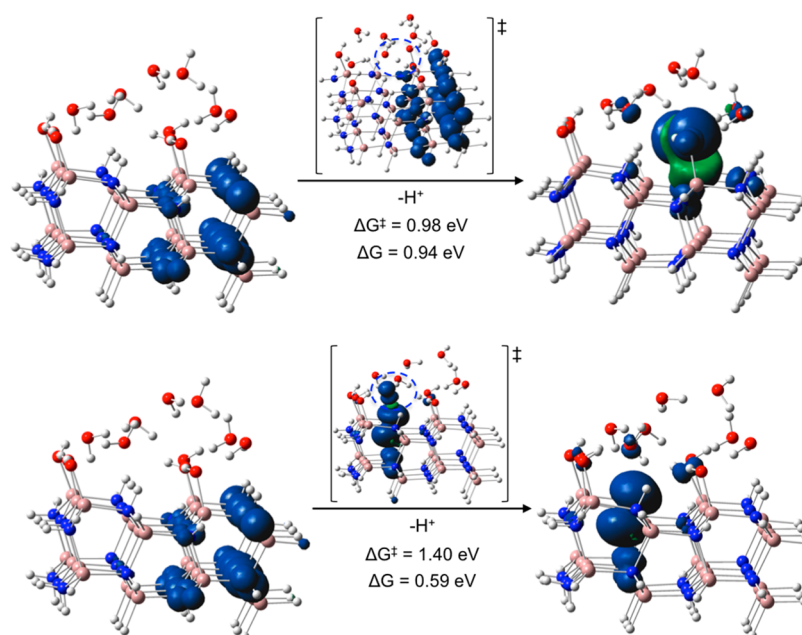


Figure 3. Atomistic models and unpaired spin densities for the one-electron oxidized cluster model along with transition state and product structures associated with deprotonation through –Ga–OH (top) and –NH (bottom) sites.

compared to those involving the –Ga–OH species, where the number of donor hydrogen bonds is virtually independent of  $d_{\text{D-A}}$ . The different strength of –Ga–OH versus –NH donor hydrogen bonds has important implications for the water oxidation mechanism as discussed in the following sections.

**Water Oxidation via Proton-Coupled Electron-Transfer (PCET) Steps.** In the cluster model study of water oxidation at the GaN (10 $\bar{1}$ 0) surface by Shen et al.,<sup>16</sup> which employed smaller clusters than the one considered in the present work, several (four or six, depending on the model) explicit water molecules formed a hydrogen-bonded layer over the dissociated water on the surface. Two of these water molecules were consumed in the water oxidation cycle, leaving a cluster with two fewer water molecules than it originally had. To return this final state to the initial state to complete a catalytic cycle, the two water molecules had to be replaced, and the free energy associated with this process was assessed equally to that of the two steps in which a water molecule was consumed. In the present work, a water molecule is added to the cluster model system before optimization of the geometry in the steps that consume water molecules. This is clear in Table 1, which presents the calculated data for the cluster model employed in the present work, by the definition of the

“system” (the current state of the active catalyst) and a “reservoir” that initially contains two water molecules and to which is added every species removed from the previous states of the system. As appropriate for a catalytic process, the catalyst (“system”) returns to its initial state at the end of the cycle, and the net reaction occurs in the reservoir.

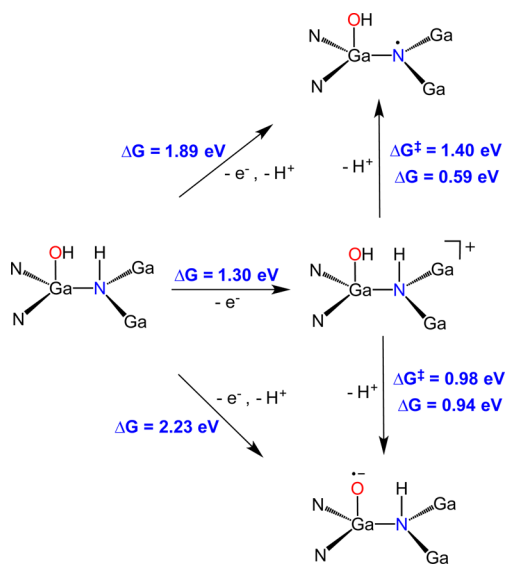
Using the cluster model approach (see Computational Methods for details), the obtained free-energy changes for the four PCET steps of water oxidation at the GaN (10 $\bar{1}$ 0) surface at pH 4.0 are 2.23, 0.94, 0.90, and 0.15 eV, respectively, at the M11-L level of theory (Table 1). The single-point calculations using the B3LYP functional on M11-L optimized structures also yielded similar free-energy changes for the PCET steps differing only by about 0.10 eV (Table S1). Comparison with the previous results by Shen et al.<sup>16</sup> indicates agreement within 0.15 eV for the PCET steps using the same basis set for H, O, and N atoms (Table S2). Moreover, the computed standard water oxidation potential is 1.06 V versus NHE at pH 4.0, in good agreement with the experimental potential of 0.99 V versus NHE at pH 4.0. The calculated  $\Delta G^{*}$  for the present cluster model (2.23 eV) shows that the first PCET step is the rate-limiting step, which determines the

thermodynamic overpotential required to make all PCET steps downhill (see the next section).

**Water Oxidation Mechanism via Decoupled PCET Steps.** Now we turn our attention to examining the mechanism of water oxidation via decoupled PCET steps at the aqueous GaN (10 $\bar{1}$ 0) interface via cluster models. We started the investigation with the first oxidation step, which occurs with an associated free-energy change of 1.30 eV. The hole generated by this oxidation delocalizes onto N atoms in the resulting positively charged system as displayed by unpaired spin density plots (Figure 3). This finding is consistent with the top of the GaN valence band being composed of N(2p) states in the periodic DFT calculations at the PBE level of theory,<sup>8</sup> but is surprising in the sense that the proposed water oxidation mechanisms for several molecular and heterogeneous catalysts involve hole localization on oxygen atoms to generate reactive species for the critical step of O–O bond formation.

Following this observation, we examined possible subsequent deprotonation steps from either an –NH site or a –Ga–OH site of the oxidized cluster. The calculated free-energy changes indicate that deprotonation from an –NH site is favored over a –Ga–OH site by 0.35 eV (0.59 eV vs 0.94 eV). In contrast, the located transition-state (TS) structures for the deprotonation events exhibit free energy of activation ( $\Delta G^\ddagger$ ) values of 1.40 and 0.98 eV for –NH and –GaOH sites, respectively (Figure 3; Scheme 1). We also performed single-point calculations at the B3LYP level of theory for the first PCET step and found very good agreement with the M11-L results (Scheme S2).

#### Scheme 1. Energetics of Proton-Coupled Electron Transfer from –NH and –Ga–OH Sites



Closer inspection of the TS structures reveals that the –NH deprotonation proceeds via proton transfer to a neighboring H<sub>2</sub>O molecule above the –NH site, resulting in the generation of an H<sub>3</sub>O<sup>+</sup> intermediate (Figure 4a), whereas the –Ga–OH deprotonation involves proton transfer to a neighboring –Ga–OH site assisted by a H<sub>2</sub>O molecule (Figure 4b). This difference essentially stems from the difference between the hydrogen-bonding network involving –NH and –Ga–OH sites as observed during the AIMD simulations in which –Ga–OH sites are always associated with water molecules as hydrogen-bonding partners, whereas –NH sites do not strongly

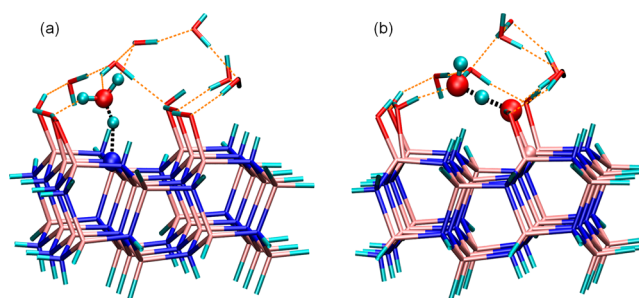


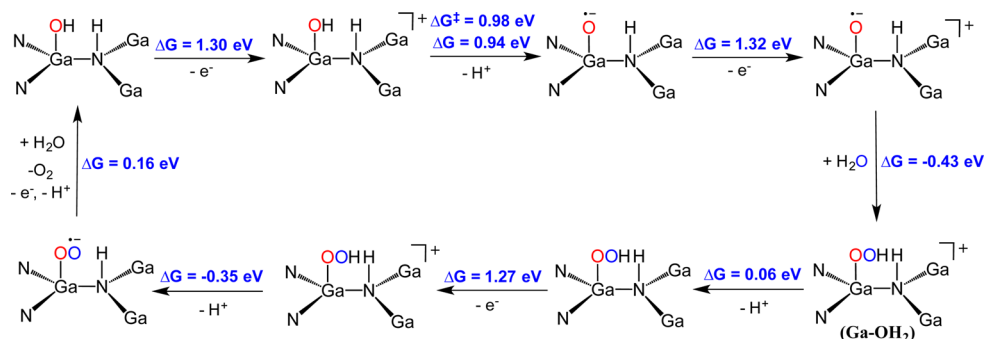
**Figure 4.** Transition state structures for deprotonation from (a) a –NH site and (b) a –Ga–OH site. Proton transfer pathways are depicted by the thick black dashed lines.

interact with H<sub>2</sub>O molecules. As a result, H<sub>2</sub>O molecules are aligned in a favorable way to accept a proton from –Ga–OH (Figure 4b), whereas deprotonation from –NH involves disturbing those favorable interactions and bringing a single water molecule into close contact with a –NH site (Figure 4a). Therefore, we propose that although deprotonation from an –NH site is favored thermodynamically, the positions and hydrogen-bonding interactions of water molecules render –Ga–OH sites more favorable kinetically toward deprotonation following the oxidation step. The spin density data indicate that upon deprotonation, the hole localizes on the oxygen atom of –Ga–O, resulting in an oxyl radical ion species, –Ga–O<sup>•-</sup> (Figure 3). Similar hole dynamics upon changes in the hydrogen-bonding pattern and deprotonation were also shown for anatase TiO<sub>2</sub>.<sup>45</sup> The calculated  $\Delta G^{*'}$  for the first coupled-electron and proton-transfer step is 2.23 eV at pH 4.0 (Table 1) and constitutes the step with the highest energy requirement for the proposed water oxidation mechanism as shown in Scheme 2, in which the free-energy changes associated with sequential PCETs, with the proton transfer (PT) following the electron transfer (ET), are presented for the overall water oxidation mechanism. Therefore, the deprotonation of surface –Ga–OH sites in the first oxidation step will be the limiting factor for the generation of reactive –Ga–O<sup>•-</sup> intermediates and consequently for overall water oxidation cycle.

The second oxidation step requires 1.32 eV and results in a delocalized hole on N atoms similar to the first oxidation step, but now with a reactive –Ga–O<sup>•-</sup> intermediate also on the surface so that a total of two oxidizing equivalents is stored in the cluster. The subsequent addition of a water molecule to generate an O–O bond is downhill by 0.43 eV. This nucleophilic addition of the H<sub>2</sub>O molecule results in the formation of a –Ga–OOH hydroperoxide intermediate and involves a proton transfer to a nearby –Ga–OH site to form a transient –Ga–OH<sub>2</sub>, from which a proton could be transferred to the bulk solution. Sequential oxidation ( $\Delta G^{*'} = 1.27$  eV) and deprotonation ( $\Delta G^{*'} = -0.35$  eV) of –Ga–OOH leads to a –Ga–OO<sup>•-</sup> superoxide intermediate, which, upon an additional oxidation, evolves molecular oxygen and regenerates the initial –Ga–OH species by the addition and dissociation of another water molecule.

## CONCLUSION

We studied the GaN (10 $\bar{1}$ 0)–water interface with AIMD simulations and examined the water oxidation mechanism following PCET steps by performing DFT calculations on cluster models. The calculated free energies for the four PCET

Scheme 2. Proposed Water Oxidation Mechanism at pH 4.0 Using Molecular Cluster Models<sup>a</sup>

<sup>a</sup>(Ga-OH<sub>2</sub>) refers to the protonation of a neighboring -Ga-OH site.

steps of the oxygen evolution reaction indicate that the first PCET step for the conversion of -Ga-OH to -Ga-O•<sup>-</sup> is associated with the highest energy requirement. Investigation of electron-transfer (ET) and proton-transfer (PT) steps separately for the first PCET reveals that deprotonation is rate limiting and that the hole localizes on an oxygen atom to generate a reactive oxyl radical ion intermediate upon deprotonation. Our calculations show that although deprotonation from -NH sites is thermodynamically more favorable upon photogenerated hole creation, the hydrogen-bonding network at the GaN (10 $\bar{1}0$ )-water interface renders deprotonation from an -OH site to be kinetically preferred. Therefore, the oxygen evolution activity will be enhanced by increasing the rate of deprotonation from -OH sites while limiting the -NH deprotonation, especially for the case of GaN/ZnO alloys for which removal of a proton from -NH sites may not be as disfavored kinetically as for GaN. Furthermore, the present work displays the strength of the coupled approach of using periodic ab initio molecular dynamics and cluster models for the investigation of the mechanism of electrocatalytic reactions on surfaces of semiconductors.

## ■ ASSOCIATED CONTENT

### Supporting Information

The following file is available free of charge on the ACS Publications website at DOI: 10.1021/acscatal.5b00054.

Schemes S1–S3, Figures S1–S4, Tables S1 and S2, and Cartesian coordinates of optimized structures from cluster models (PDF)

## ■ AUTHOR INFORMATION

### Corresponding Authors

\*(J.T.M.) E-mail: muckerma@bnl.gov.

\*(M.Z.E.) E-mail: msertem@bnl.gov.

\*(N.K.) E-mail: nkharce@bnl.gov.

### Author Contributions

<sup>||</sup>M.Z.E. and N.K. contributed equally.

### Notes

The authors declare no competing financial interest.

## ■ ACKNOWLEDGMENTS

The work carried out at Brookhaven National Laboratory was supported by the U.S. Department of Energy, Office of Science, its Office of Basic Energy Sciences (Computational Materials and Chemical Sciences Network program, Division of Chemical Sciences, and Scientific User Facilities Division), under

Contract DE-SC00112704 and utilized resources at the Center for Functional Nanomaterials, Brookhaven National Laboratory, and at the National Energy Research Scientific Computing Center, supported by the Office of Science of the U.S. Department of Energy under Contract DE-AC02-05CH11231. J.C.T. acknowledges support by the U.S. Department of Energy, Office of Science, its Office of Basic Energy Sciences, under Contract DE-FG02-05ER15677. V.S.B. acknowledges support as part of the Argonne–Northwestern Solar Energy Research (ANSER) Center, an Energy Frontier Research Center funded by the U.S. Department of Energy, Office of Science, Office of Basic Energy Sciences, under Award DE-SC0001059.

## ■ REFERENCES

- (1) Lewis, N. S.; Nocera, D. G. *Proc. Natl. Acad. Sci. U.S.A.* **2006**, *103*, 15729–15735.
- (2) Gust, D.; Moore, T. A.; Moore, A. L. *Acc. Chem. Res.* **2009**, *42*, 1890–1898.
- (3) Armadori, N.; Balzani, V. *ChemSusChem* **2011**, *4*, 21–36.
- (4) Dau, H.; Limberg, C.; Reier, T.; Risch, M.; Roggan, S.; Strasser, P. *ChemCatChem* **2010**, *2*, 724–761.
- (5) Maeda, K.; Takata, T.; Hara, M.; Saito, N.; Inoue, Y.; Kobayashi, H.; Domen, K. *J. Am. Chem. Soc.* **2005**, *127*, 8286–8287.
- (6) Maeda, K.; Teramura, K.; Lu, D. L.; Takata, T.; Saito, N.; Inoue, Y.; Domen, K. *Nature* **2006**, *440*, 295–295.
- (7) Ohno, T.; Bai, L.; Hisatomi, T.; Maeda, K.; Domen, K. *J. Am. Chem. Soc.* **2012**, *134*, 8254–8259.
- (8) Jensen, L. L.; Muckerman, J. T.; Newton, M. D. *J. Phys. Chem. C* **2008**, *112*, 3439–3446.
- (9) Wang, S. Z.; Wang, L. W. *Phys. Rev. Lett.* **2010**, *104*, No. 065501.
- (10) McDermott, E. J.; Kurmaev, E. Z.; Boyko, T. D.; Finkelstein, L. D.; Green, R. J.; Maeda, K.; Domen, K.; Moewes, A. *J. Phys. Chem. C* **2012**, *116*, 7694–7700.
- (11) Liu, J.; Pedroza, L. S.; Misch, C.; Fernandez-Serra, M. V.; Allen, P. B. *J. Phys. Condens. Mater.* **2014**, *26*, No. 274204.
- (12) Xiong, A. K.; Yoshinaga, T.; Ikeda, T.; Takashima, M.; Hisatomi, T.; Maeda, K.; Setoyama, T.; Teranishi, T.; Domen, K. *Eur. J. Inorg. Chem.* **2014**, *4*, 767–772.
- (13) Maeda, K.; Teramura, K.; Saito, N.; Inoue, Y.; Domen, K. *Bull. Chem. Soc. Jpn.* **2007**, *80*, 1004–1010.
- (14) Wang, D. F.; Pierre, A.; Kibria, M. G.; Cui, K.; Han, X. G.; Bevan, K. H.; Guo, H.; Paradis, S.; Hakima, A. R.; Mi, Z. T. *Nano Lett.* **2011**, *11*, 2353–2357.
- (15) Kibria, M. G.; Nguyen, H. P. T.; Cui, K.; Zhao, S. R.; Liu, D. P.; Guo, H.; Trudeau, M. L.; Paradis, S.; Hakima, A. R.; Mi, Z. T. *ACS Nano* **2013**, *7*, 7886–7893.
- (16) Shen, X. A.; Small, Y. A.; Wang, J.; Allen, P. B.; Fernandez-Serra, M. V.; Hybertsen, M. S.; Muckerman, J. T. *J. Phys. Chem. C* **2010**, *114*, 13695–13704.

- (17) Li, L.; Muckerman, J. T.; Hybertsen, M. S.; Allen, P. B. *Phys. Rev. B* **2011**, *83*, No. 134202.
- (18) Rossmeis, J.; Qu, Z. W.; Zhu, H.; Kroes, G. J.; Norskov, J. K. *J. Electroanal. Chem.* **2007**, *607*, 83–89.
- (19) Man, I. C.; Su, H. Y.; Calle-Vallejo, F.; Hansen, H. A.; Martinez, J. I.; Inoglu, N. G.; Kitchin, J.; Jaramillo, T. F.; Norskov, J. K.; Rossmeis, J. *ChemCatChem* **2011**, *3*, 1159–1165.
- (20) Akimov, A. V.; Muckerman, J. T.; Prezhdo, O. V. *J. Am. Chem. Soc.* **2013**, *135*, 8682–8691.
- (21) Kharche, N.; Hybertsen, M. S.; Muckerman, J. T. *Phys. Chem. Chem. Phys.* **2014**, *16*, 12057–12066.
- (22) Kharche, N.; Muckerman, J. T.; Hybertsen, M. S. *Phys. Rev. Lett.* **2014**, *113*, No. 176802.
- (23) Blochl, P. E. *Phys. Rev. B* **1994**, *50*, 17953–17979.
- (24) Kresse, G.; Furthmuller, J. *Phys. Rev. B* **1996**, *54*, 11169–11186.
- (25) Kresse, G.; Joubert, D. *Phys. Rev. B* **1999**, *59*, 1758–1775.
- (26) Dudarev, S. L.; Botton, G. A.; Savrasov, S. Y.; Humphreys, C. J.; Sutton, A. P. *Phys. Rev. B* **1998**, *57*, 1505–1509.
- (27) Dion, M.; Rydberg, H.; Schroder, E.; Langreth, D. C.; Lundqvist, B. I. *Phys. Rev. Lett.* **2004**, *92*, No. 246401.
- (28) Klimes, J.; Bowler, D. R.; Michaelides, A. *Phys. Rev. B* **2011**, *83*, No. 195131.
- (29) Peverati, R.; Truhlar, D. G. *J. Phys. Chem. Lett.* **2012**, *3*, 117–124.
- (30) Peverati, R.; Truhlar, D. G. *J. Chem. Phys.* **2012**, *136*, No. 134704.
- (31) Marenich, A. V.; Cramer, C. J.; Truhlar, D. G. *J. Phys. Chem. B* **2009**, *113*, 6378–6396.
- (32) Bergner, A.; Dolg, M.; Kuchle, W.; Stoll, H.; Preuss, H. *Mol. Phys.* **1993**, *80*, 1431–1441.
- (33) Leininger, T.; Berning, A.; Nicklass, A.; Stoll, H.; Werner, H. J.; Flad, H. J. *Chem. Phys.* **1997**, *217*, 19–27.
- (34) Hehre, W. J.; Radom, L.; Schleyer, P. v. R.; Pople, J. A. *Ab Initio Molecular Orbital Theory*; Wiley: New York, 1986.
- (35) Frisch, M. J.; Trucks, G. W.; Schlegel, H. B.; Scuseria, G. E.; Robb, M. A.; Cheeseman, J. R.; Scalmani, G.; Barone, V.; Mennucci, B.; Petersson, G. A.; Nakatsuji, H.; Caricato, M.; Li, X.; Hratchian, H. P.; Izmaylov, A. F.; Bloino, J.; Zheng, G.; Sonnenberg, J. L.; Hada, M.; Ehara, M.; Toyota, K.; Fukuda, R.; Hasegawa, J.; Ishida, M.; Nakajima, T.; Honda, Y.; Kitao, O.; Nakai, H.; Vreven, T.; Montgomery, J. A.; Peralta, J. E.; Ogliaro, F.; Bearpark, M.; Heyd, J. J.; Brothers, E.; Kudin, K. N.; Staroverov, V. N.; Kobayashi, R.; Normand, J.; Raghavachari, K.; Rendell, A.; Burant, J. C.; Iyengar, S. S.; Tomasi, J.; Cossi, M.; Rega, N.; Millam, J. M.; Klene, M.; Knox, J. E.; Cross, J. B.; Bakken, V.; Adamo, C.; Jaramillo, J.; Gomperts, R.; Stratmann, R. E.; Yazyev, O.; Austin, A. J.; Cammi, R.; Pomelli, C.; Ochterski, J. W.; Martin, R. L.; Morokuma, K.; Zakrzewski, V. G.; Voth, G. A.; Salvador, P.; Dannenberg, J. J.; Dapprich, S.; Daniels, A. D.; Farkas, Ö.; Foresman, J. B.; Ortiz, J. V.; Cioslowski, J.; Fox, D. J. *Gaussian 09*, revision A.02; Gaussian, Inc.: Wallingford, CT, USA, 2010.
- (36) Cramer, C. J. *Essentials of Computational Chemistry: Theories and Models*, 2nd ed.; Wiley: Chichester, UK, 2004; pp 385–427.
- (37) Tissandier, M. D.; Cowen, K. A.; Feng, W. Y.; Gundlach, E.; Cohen, M. H.; Earhart, A. D.; Coe, J. V.; Tuttle, T. R. *J. Phys. Chem. A* **1998**, *102*, 7787–7794.
- (38) Camaioni, D. M.; Schwerdtfeger, C. A. *J. Phys. Chem. A* **2005**, *109*, 10795–10797.
- (39) Kelly, C. P.; Cramer, C. J.; Truhlar, D. G. *J. Phys. Chem. B* **2006**, *110*, 16066–16081.
- (40) Bryantsev, V. S.; Diallo, M. S.; Goddard, W. A. *J. Phys. Chem. B* **2008**, *112*, 9709–9719.
- (41) Lewis, A.; Bumpus, J. A.; Truhlar, D. G.; Cramer, C. J. *J. Chem. Educ.* **2004**, *81*, 596–604 (erratum **2007**, *84*, 934); 10.1021/ed081p596
- (42) Winget, P.; Cramer, C. J.; Truhlar, D. G. *Theor. Chem. Acc.* **2004**, *112*, 217–227.
- (43) Becke, A. D. *J. Chem. Phys.* **1993**, *98*, 5648–5652.
- (44) Wang, J.; Pedroza, L. S.; Poissier, A.; Fernandez-Serra, M. V. *J. Phys. Chem. C* **2012**, *116*, 14382–14389.
- (45) Chen, J.; Li, Y. F.; Sit, P.; Selloni, A. *J. Am. Chem. Soc.* **2013**, *135*, 18774–18777.